Atmos. Meas. Tech. Discuss., 5, 1253–1292, 2012
www.atmos-meas-tech-discuss.net/5/1253/2012/
doi:10.5194/amtd-5-1253-2012

Atmospheric Measurement Techniques Discussions

The RAMNI airborne lidar for cloud and aerosol research

F. Cairo[1], G. Di Donfrancesco[2], L. Di Liberto[1], and M. Viterbini[1]

[1]Istituto di Scienze dell'Atmosfera e del Clima, Consiglio Nazionale delle Ricerche, Roma, Italy
[2]Ente Nazionale per le Nuove tecnologie, l'Energia e l'Ambiente, Roma, Italy

Received: 30 December 2011 – Accepted: 18 January 2012 – Published: 9 February 2012

Correspondence to: F. Cairo (f.cairo@isac.cnr.it)

Published by Copernicus Publications on behalf of the European Geosciences Union.

Abstract

We describe an airborne lidar for the characterization of atmospheric aerosol. The system has been set up in response to the need to monitor extended regions where the air traffic may be posed at risk by the presence of potentially harmful volcanic ash, and to study the characteristics of volcanic emissions both near the source region and when transported over large distances. The lidar provides backscatter and linear depolarization profiles at 532 nm, from which aerosol and cloud properties can be derived. The paper presents the characteristics and capabilities of the lidar system and gives examples of its airborne deployment. Observations from three flights, aimed at assessing the system capabilities in unperturbed atmospheric conditions, and at characterizing the emissions near a volcanic ash source region, the Mt. Etna, and transported far away from the source, are presented and discussed.

1 Introduction

The lidar technique has high potentials for assessing the particulate burden in the atmosphere, since is currently the only remote sensing system that allows the direct determination of the vertical profiles of optical properties of micron-sized aerosols and particles in thin clouds. Due to new powerful laser sources and improved electronics, profiles of the optical properties of the atmosphere can be achieved with high spatial and temporal resolution, tipically of the order of metres, and of seconds. Such high resolution allows both to monitor the temporal evolution of the stratification and dynamics of aerosols in the atmosphere above a ground-based station, and to sample extended regions, when the instrument is mounted on moving platforms such as vans, ships or aircraft (Lilley et al., 2004). Airborne lidars have been used since the early eighties (Moerl et al., 1981; Rengel et al., 1997; Flamant et al., 2000) and now reliable, robust, transportable systems are widely used throughout the world, deployed in remote sites in harsh conditions, on board of both large (Stachlewska et al., 2010) or

AMTD
5, 1253–1292, 2012

ultralight (Chazette et al., 2007) aircraft. The capability of airborne lidar to measure the atmospheric particulate in real time over extended regions, has demonstrated its great usefulness in response to the recent emergency, induced by the Eyjafjalla volcano eruption between April and May 2010 (Petersen, 2010). Then, the volcanic plume originated from the eruption, dwelled over Europe for several weeks, hampering the civil air traffic and perturbing the economic, political and cultural activities of the continent. Consequently, several airborne lidar usually devoted to atmospheric research were deployed to perform measurements of aerosols and volcanic ashes (Schumann et al., 2011; Marenco et al., 2011). That effort of the scientific community toward monitoring and quantifying the presence of ash, had the twofold goal both to study the evolution and fate of the volcanic plume (Bukowiecki et al., 2011; Ansmann et al., 2011), and to provide input to decision makers that had to face such civil contingency.

Lidar can easily detect the presence of volcanic ash, identified by using polarization diversity and/or multi-wavelenght backscatter systems. The amount of ash can then be assessed under some assumption on particle size spectrum, refractive index and density (Ansmann et al., 2010). Such information, provided in real time, allowed to validate the reports and forecasts of the movement of the volcanic ash cloud, issued by the Volcanic Ash Advisory Centres, and to inform the national Civil Aviation Authorities that had to issue warnings for the flight safety over extended areas, possibly affected by ash presence.

Triggered by the need to provide adequate coverage to the national territory, in May 2010 the Italian civil aviation authority asked our Institution to set up an airborne lidar capable to detect and quantify the presence of particulate and ashes in the atmosphere. A lidar (RAMNI – Radar ottico Aviotrasportato per il Monitoraggio delle No-flight zones sopra IItalia – Airborne Optical radar for monitoring No-Flight Zones over Italy) has then been certified to fly, installed and tested on an Alenia C-27J Spartan, a medium-sized transport aircraft of the Italian Air Force. Such system is now operative and obeys the twofold role of providing the atmospheric science community with a research instrument tested for airborne operations, and to deliver operatively

AMTD
5, 1253–1292, 2012

real-time estimates of the volcanic ash burden in the atmosphere, in case of civil contingencies. The present work describes the characteristics of the RAMNI system and the data analysis procedure, and illustrates some of its observations. Results from flights aimed at testing the capabilities of the system and at detecting the presence of ashes emitted from Mt. Etna, and from Grimsvotn volcanoes are here presented and discussed.

2 Instrument description

The RAMNI lidar that has been installed on the C-27J, belongs to the instrumental equipment usually deployed in experimental station of San Pietro Capofiume (11.6° E, 44.7° N), mantained by the Institute of Atmospheric Sciences and Climate of the italian National Research Council. It was designed and implemented in the framework of a collaboration between ISAC-CNR, the Ente Nazionale per le Nuove tecnologie, l'Energia e l'Ambiente (ENEA) and Embedded Devices s.r.l (now IsoComp, www.isocomp.it), an italian SME. Systems sharing some common feature with the one hereby described have been used in remote sites in Africa (Cavalieri et al., 2011, 2010) and Spitzberger (Di Liberto et al., 2012). The system, designed for unattended outdoor use, is contained in a 30 × 40 × 50 cm aluminum box, electronically shielded and thermally insulated with polyurethane. A quartz window allows the transmission of the laser pulse toward the atmosphere, and the collection of the backscattered signal. The temperature in the aluminium box is controlled by four cooler-heater Peltier cells, 20 W each, which maintain the temperature within the laser operating conditions (10 °C–30 °C). The system power consumption is less than 240 W (10 A at 24 V).

2.1 Transmitter

The laser (Bright Solutions, Wedge) is an air cooled, diode pumped Nd-YAG, with second-harmonic generation and active *Q* switching. The laser pulse duration is 1 ns

AMTD
5, 1253–1292, 2012

and the emission is on two wavelengths, with energies of 350 µJ/pulse at 532 nm (green) and 800 µJ/pulse at 1064 nm (near infrared). The pulse repetition rate is 1 kHz. From factory specifications, the laser beam divergence is 3 mrad and is further reduced by a factor of 7 by a beam expander. The half divergence sdiv of the laser has been measured in the field, by following horizontally the diverging beam cross section in an open field, for a distance of 350 m. The beam cross section resulted to be elliptical, and its divergence was different along the two main axes. The measured minimum value of the two half divergences was 0.2 mrad. This leads to a decrease of the energy density *S(r)* across the beam cross section with the distance *r* from the source, that decreases more rapidly than

$$S(r) = \frac{E}{r^2 \cdot \mathrm{sdiv}} \quad (1)$$

where E is the pulse energy. This equation allowed us to define the minimum safety distance beyond which the laser beam is considered eye safe. Eye safety is a major concern for both nadir or zenith pointing airborne lidars, and is further discussed and detailed in Appendix A. The laser beam is sent into the atmosphere by means of a steerable dielectric mirror, placed before the beam expander. The mirror positioner allows fine alignments of the beam with respect to the telescope field of viev (FOV).

2.2 Receiver

The optical receiver is a Newtonian telescope with a diameter of 20 cm, f/1.5, with a FOV of 0.75 mrad, regulated by a pinhole of 200 µm placed in the telescope focal plane, acting as field stop. Under this geometry, the overlap of the laser beam with the telescope FOV begins at 40 m from the instrument and is completed at 600 m.

A gray photochromic glass is placed in the telescope focal plane, to reduce the efficiency of the system by a factor of 4 under conditions of strong sky background light; this in order to moderate the effects of saturation and non linearity on the light detectors. The backscattered light is collimated and spectrally split by low-pass dichroic

AMTD
5, 1253–1292, 2012

cubes, and then filtered by narrow band interference filters, with 2 nm bandwidth (Semrock) to separate the backscatter at 532 nm, at 608 nm – the Raman scattering from nitrogen – and 1064 nm. These filters have high transmission (≥90 %) and a negligible temperature dependence. A cube polarizer is used to further divide the radiation at 532 nm in the components parallel and perpendicular to the plane of polarization of the emitted light. The radiation at 608 and 532 nm is directed on miniature photomultiplier modules (Hamamatsu 5783P and 6780-20 respectively) with very low thermal noise (less than 10 counts s^{-1} at 25 °C). The 1064 nm radiation is focused into an Avalanche Photo Diode (APD) C30954E (EGG) with 0.8 mm photo sensitive area diameter. The polarization voltage for the APD is set manually to a suitable value by a custom electronic board. This electronics allows to keep the APD gain fixed, by automatically varying the polarization voltage and hooking it to possible APD temperature changes, in accordance with the APD gain vs. temperature curve.

2.3 Data acquisition

The signal from the photodetectors is amplified with a gain of 11 and a bandwidth of 250 MHz. As usual in photomultiplier detection, two cases arises: if the photon arrival rate is such that the electrical impulses, originated by the single photon detection process, pile up to produce a continuous current waveform, the signal is measured in *current mode*; if otherwise the photon arrival rate is low enough to allow to discriminate the electrical impulses originating from a single photon detection, the signal is measured in *photoncounting mode*. In our case, the signal is simultaneously recorded both in current and in photocounting mode, and the two acquisitions are then suitably merged when the data are processed, as detailed hereafter. The electronic acquisition card (Embedded Devices, APC-80250DSP) is based on FPGA technology and uses a fast digital signal processor unit (DSP) for both modes. In current mode, the photomultiplier signal is filtered through a 15 MHz low pass to avoid aliasing effects, and then digitized into an 8 bits waveform, at an adjustable sampling rate. The duration of the single sample can be adjusted to the values of 12.5, 25, 50 or 100 ns, and the waveform

AMTD
5, 1253–1292, 2012

is reconstructed for a total of 1024 samples, i.e. for a time duration of respectively 12.8, 25.6, 51.2 and 102.4 µs. This delivers a reconstruction of the profile that extends for 1.85, 3.75, 7 and 15 km, with a spatial resolution of 1.875, 3.75, 7.5 and 15 m. The first 50 samples are collected before the laser shot and are used to measure the sky background.

In photoncounting mode the impulses originating from photon detection are counted when they reach an adjustable threshold level, that allows to reject spurious low noise. For each photon detection, TTL pulses ar formed and counted in 1024 consecutive time bins, whose length may span from 25 to 1000 ns in 25 ns increments. This allows to reconstruct the profile of the atmospheric backscatter extending for 7.5 km at the least, and 150 km at the most, this length adjustable in 7.5 km steps. Similarly, the vertical resolution is adaptable from 7.5 m up to 150 m, in 7.5 m steps. The acquisition card provides the sum of the signals, integrated over N laser shots. Thus, profiles are produced as averages over times that can range from 1 s (i.e. a minimum of 1000 laser shots, whereas the frequency of laser pulses is 1 kHz) to several tens of hours, and the averaging time can be adjusted by means of the control software. A good compromise between good signal to noise ratio and a sufficient temporal resolution is generally obtained by setting the time average to 5 s. Averaged profiles are stored in the memory board of the system (500 MB, expandible to several GB), which can to accumulate tens of thousands of them. An external computer is used to access the system, and a dedicated software package allows to modify the settings of the acquisition card (average profile duration, its vertical extension and resolution, frequency and power of the laser pulse, photoncounting threshold level and so on) via USB or TCP/IP connection. The system automatically starts operating and storing data as it gets turned on, and stops when it is turned off, or whenever an appropriate command is sent from an external computer, as, for instance, when it is necessary to stop the data logging to download the data or to provide real-time data visualization for alignment purpose. Data are stored as ASCII files. Each file reports information on the system settings, and the raw data as series of photocounts per bin and averaged current waveforms, in digit units.

AMTD
5, 1253–1292, 2012

A real time visualization of the measurements is possible on an external computer by means of a suitable software package, for system checking or for alignment. A synopsis of the system specifications is reported in Table 1. The photoncounting mode, preferable in the acquisition of atmospheric returns from distant ranges due to better signal to noise ratio and absence of spurious electronic biases, tends to get saturated in bright daylight, or in the acquisition of atmospheric returns from regions close to the instrument. In these conditions, use of the current mode is mandatory. A vertical region of overlap between current and photoncounting mode acquisitions exists, and allows merging the two to reconstruct the whole backscattering profile from a few tens of meters from the instrument to the maximum altitude of the sounding. The region where the two acquisition modes coexist and are both accurate and sensitive, is placed generally between 2 km and the top of the current mode profile, which can be at 3.75 km or higher. In this region, the photoncounting mode has still a good linearity and current mode is sensitive enough.

2.4 Uncertainty analysis

We here discuss the uncertainty to be attributed to the measurements, following the well established literature on the lidar error analysis (Russell et al., 1979), which we here briefly summarize. Let $N(r)$ be the number of photons generated by the process of backscatter at a distance r from the system and detected by our lidar system, in case of photoncounting detection, or a current directly proportional to them in case of current detection; let E the energy of the laser pulse, C a parameter that describes the overall efficiency of the system, $\beta(r)$ and $\alpha(r)$ respectively the backscatter coefficient and atmospheric extinction. We have:

$$N(r) = \frac{E \cdot C \cdot \beta(r)}{r^2} \cdot \exp(-2 \cdot \int_0^r \alpha(r) dr) = \\ = \frac{E \cdot C \cdot \beta(r)}{r^2} \cdot T(r) \quad (2)$$

AMTD
5, 1253–1292, 2012

Where it is understood that in the case of elastic scattering, extinction and backscatter coefficients can be divided into a contribution due to air molecules and aerosol:

$$\beta(r) = \beta_m(r) + \beta_a(r) \quad (3)$$

$$\alpha(r) = \alpha_m(r) + \alpha_a(r) \quad (4)$$

A quantity commonly used in lidar research is the total Backscatter Ratio R

$$R(r) = \frac{\beta(r)}{\beta_m(r)} \quad (5)$$

defined so that $R = 1$ if there are no aerosols, and $R \geq 1$ otherwise. This is rewritten in terms of measured quantities as:

$$R(r) = \frac{N(r) \cdot r^2}{E \cdot C \cdot \beta_m(r) \cdot T(r)} \quad (6)$$

The system parameters E and C are eliminated by a calibration procedure that assumes as known the value $R_0 = R(r_0)$ at a given calibration altitude r_0. Then:

$$R(r) = \frac{N(r) \cdot r^2 \cdot \beta_m(r_0) \cdot T(r_0)}{N(r_0) \cdot r_0^2 \cdot \beta_m(r) \cdot T(r)} \quad (7)$$

and once $R(r)$ is retrieved from the measurements, we finally get to the quantity of physical interest, the aerosol volume backscatter coefficient:

$$\beta_a(r) = (R(r) - 1) \cdot \beta_m(r) \quad (8)$$

that, introducing the parameters:

$$n(r) = \frac{N(r)}{N(r_0)}; x = \frac{r}{r_0}; q = \frac{T(r_0)}{T(r)}; \beta_m(r_0) = {\beta_m}^0 \quad (9)$$

AMTD
5, 1253–1292, 2012

takes the form:

$$\beta_a(r) = n(r)\cdot x\cdot q\cdot\beta_m^0\cdot R_0 - \beta_m(r) \quad (10)$$

To which we can assign a relative uncertainty given by:

$$\left(\frac{\delta\beta_a}{\beta_a}\right)^2 = \left(\frac{\beta_m\cdot R}{\beta_a}\right)^2\cdot\left[\left(\frac{\delta n}{n}\right)^2 + \left(\frac{\delta x}{x}\right)^2 + \left(\frac{\delta q}{q}\right)^2 + \left(\frac{\delta\beta_m^0}{\beta_m^0}\right)^2 + \left(\frac{\delta R_0}{R_0}\right)^2 + \frac{1}{R^2}\cdot\left(\frac{\delta\beta_m}{\beta_m}\right)^2 - \frac{2\cdot c^2}{\beta_m^0\cdot\beta_m\cdot R}\right] \quad (11)$$

We now quantify the individual contributions to be applied to our system: $(\frac{\delta n}{n})$ is the uncertainty on the measured signal: it has a fixed contribution due to the statistics of photons arriving from the calibration altitude r_0, which we often place around 6–7 km, and a contribution varying along the profile.

We detail the discussion for the two different modes of detection: if the signal is detected in photocounting mode, then n is proportional to the sum of photoncounts arrived and detected during each serie of consecutive time bins. The Poissonian statistics of photon arrival gives the standard deviation as the square root of the number of photoncounts. Each laser shot causes a burnst of backscattered photons, and averaging N of such burnsts is a common way to increase the counting statistics, thus improving the signal to noise ratio by a factor $\sqrt{N}$. In our case, tipical averaging times range from 5 to 60 s, so that, given our laser pulse repetition rate, N may range from 5000 to 60 000. As detailed in Sect. 2.3, photoncounting is performed over a serie of 1028 consecutive time bins of adjustable width. In the measurements presented hereafter, the width of such bins was set to 200 ns (and consequently the vertical resolution of our profile to 30 m, and its extent to 30 km). If *bkg* is the sky background photon count and p is the overall photon count, the uncertainty on the lidar signal $n = p - b$ will be $\frac{\delta n}{n} = \frac{\delta p}{n} + \frac{\delta bkg}{n}$. Even in daylight, for our sistem, the sky background photon count rate is some 10^6 photoncount s^{-1} and is negligible throughout a large part of the tropospheric return.

AMTD
5, 1253–1292, 2012

In current mode the waveform is digitized with an 8-bits Analog to Digital Converter (ADC), and recorded. The digital resolution error, on the single sample, is equal to its least significant bit (LSB). On an average of N samples, as the LSB is dithered by noise from electronics and from inherent atmospheric variabiliy, the averaged waveform resolution is increased by a factor $\sqrt{N}$ corresponding to an increment of $\frac{\log_2 N}{2}$ bits. In our case, for $N = 5000$, the averaged waveform has an equivalent LSB of 14 bits; for $N = 60\,000$ the equivalent LSB is 16 bits. As above, if *bkg* is the current caused by the sky background, or by any other electronic bias, and p the overall current, $n = p - bkg$ and the uncertainty on the lidar signal will be $\frac{\delta n}{n} = \frac{\delta p}{n} + \frac{\delta bkg}{n}$. Practically, the digital uncertainty is usually much smaller than the uncertainty arising from the determination of *bkg*. In fact, this is computed as the average current level of the waveform in the 50 samples preceding the laser shot. Such current level is "noisy", due to electronics as well as inherent signal variability, so that the standard deviation STD_{bkg} of the sky backgroung level is usually greater than the digital resolution error, in every condition. Such standard deviation, taken as the uncertainty on the sky background signal, can be though to affect equally every other portion of the current waveform, and so we put $\delta p = \delta bkg = \mathrm{STD}_{bkg}$.

$\frac{\delta x}{x}$ is the uncertainty on altitude, which we consider negligible.

$\frac{\delta q}{q}$ is the error on the transmission. In the worse case, when the Raman channel is too noisy – as, for our system, in daylight conditions – no other indipendent extinction measurement is available and only one wavelenght is used in the retrieval algorithm, β_a can be calculated only if a priori assumptions are made on the relation between aerosol extinction and backscatter coefficients (the so-called *lidar ratio*). In such assumptions lie the largest source of uncertainty in the retrieval: following the literature, (Russell et al., 1979; Bockmann et al., 2004) we write:

$$\left(\frac{\delta q}{q}\right)^2 = 4\cdot(\delta\tau_\mathrm{a}^2 + \delta\tau_\mathrm{m}^2) \cong 4\cdot((0.5\cdot\tau_\mathrm{a})^2 + (0.1\cdot\tau_\mathrm{m})^2) \quad (12)$$

where $\tau_{\mathrm{a,m}}$ indicate the optical depths due to aerosol and molecules, respectively.

AMTD
5, 1253–1292, 2012

$\frac{\delta\beta_m^0}{\beta_m^0}$ and $\frac{\delta\beta_m}{\beta_m}$ both reflect uncertainties on the molecular density, derived from other independent measurements or a suitable atmospheric model. In our case we put both of them equal to 0.01.

$\frac{\delta R_0}{R_0}$ is the uncertainty on the $R(r_0)$ calibration value used in the retrieval; in our case, it is often possible to reach in a measurement session the upper part of the troposphere where the molecular scattering dominates. A conservative estimation is to put the uncertainty on R_0 at 0.02.

Finally, the term $\frac{2 \cdot c^2}{\beta_m^0 \cdot \beta_m \cdot R}$ that takes into account the error covariance between the density of the molecular profile at the altitude of calibration, is neglected. This will induce a negligible overestimation of the error at the altitude of calibration.

We will use the result here discussed to calculate the uncertainty of the measurements presented hereafter, and hence the minimum detectable aerosol backscatter coefficient.

2.5 Data processing

The system is able to measure the atmospheric return backscattered elastically at 1064 nm, at 532 nm in parallel and perpendicular polarization, and the nitrogen Raman scattered signal at 608 nm, although this latter is available only at night due to the low value of its scattering cross section. Unfortunately, for the measurements acquired during the flights presented hereafter, the 1064 nm data were plagued by a spurious noise that hampered their use in a quantitative way. We will present and quantitatively discuss here only the data acquired with the polarization diversity 532 nm channels, and in the following, an outline of the data processing will be given. The preliminary step in the data processing procedure is the correction for dead time effects on the photoncounting mode profiles. According to Donovan et al. (1993), let S_0 the true photocounting rate, and S_v the photocounting rate observed by our device, the two are linked by;

$$S_v = S_0 \cdot \exp(-S_0 \cdot \tau) \quad (13)$$

AMTD
5, 1253–1292, 2012

where the dead time τ can be estimated from the maximum observed photocounting rate as $\tau = \frac{1}{S_v^{max} \cdot e}$ and in our case is 6 ns. Equation (13) allows the retireval of the true photoncounting rate, and this extends some hundreds of metres down the limit where the photoncounting profile can be considered accurate. The part of the profile further down, generally below 1 km in daylight, or even further down at night-time, where the correction would exceeds 50 %, is considered not reliable.

The current mode profile is corrected for the partial overlap between the laser beam and the FOV in the near range, so that the signal in the near range is reconstructed using the procedure described in Biavati et al. (2011). The correction is considered reliable if it does not exceed 75 % of the reconstructed signal. In this way, an atmospheric profile is retrieved down to 100–200 m from the instrument. The current and photoncounting profiles are then superimposed and merged together in a region where both acquisition modes are considered sensitive and accurate, generally above 2–3 km in daylight, so that a single atmospheric profile is created for each channel, with data below the merging region acquired in current mode, and data above that in photocounting mode. Figure 1 displays the atmospheric backscatter signal acquired on a clear night with 300 s integration time. The figure reports the atmospheric return as photoncounting rates per single laser shot. The photocounting mode acquisition is presented before (black line) and after (blue line) the application of the dead time correction, the current mode acquisition is displayed before (red line) and after (purple line) the application of the partial overlap correction. Also displayed are the altitude regions where the overlapping photoncounting and current signals are merged, and the region used for calibrating the signal. The reconstructed profile, once divided for the photon rate arriving from the calibration altitude r_0 delivers the quantity $n(r)$ in Eq. (9) which is the basis for further processing.

AMTD
5, 1253–1292, 2012

2.5.1 Aerosol backscatter coefficient

The molecular backscatter in Eq. (10) and the molecular extinction coefficient can be evaluated from Rayleigh scattering theory once the air density profile is obtained from independent measurements or from a suitable atmospheric model. Since both the aerosol backscatter and extinction coefficient are present in Eq. (10) as unknown, we follow the standard Klett approach (Klett, 1981) and assume a relation between them, the so-called extinction to backscattering ratio, or *lidar ratio*, in order to invert the lidar equation. Our choice is to fix the lidar ratio to piecewise constant values in regions where clouds or aerosols were present. Such regions were identified by iteratively inspecting the values of backscatter ratio, depolarization ratio and altitude during the data processing, and recursively adjusting the lidar ratio accordingly. As instance, when thin liquid or ice clouds were identified in a given altitude range, the lidar ratio there was set to values known from literature (Chen et al., 2002; O'Connor et al., 2004). The lidar ratio for aerosol may easily range from 30–50 sr^{-1} in the case of dust (Mattis et al., 2002; Immler et al., 2003) to 80 sr^{-1} for biomass burning aerosol (Wandinger et al., 2002), and reported values for volcanic ashes are in the range 50–60 (Ansmann et al., 2010). Although our data process allow to constrain the aerosol lidar ratio value when additional co-located Aerosol Optical Depth measurements from sunphotometers are available (as in the San Pietro Capofiume station) (Marenco et al., 1997), or to provide an altitude dependent aerosol lidar ratio when the nitrogen Raman signal (Ansmann et al., 1990) is available during nighttime, these opportunities were not available during the flight test, performed in daylight. Hence a constant aerosol lidar ratio was set to 50 sr^{-1} everywhere, except when cirrus (30 sr^{-1}) or thin water clouds (19 sr^{-1}) were identified.

2.5.2 Aerosol depolarization

The volume linear depolarization ratio δ is defined as the ratio of the perpendicular to the parallel-polarized lidar return signal, with respect to the plane of polarization of

AMTD
5, 1253–1292, 2012

the transmitted linearly polarized laser light. It is an important parameter that allows discrimination of various kind of aerosol and clouds (Sassen, 1991; di Sarra et al., 2001; Iwasaka et al., 2003). In principle, it can be directly evaluated from the powers recorded on the two receiving channels *par* and *cross*, detecting the lidar return once split according to its polarization diversity.

$$\delta(r) = K \cdot \frac{n^{\text{cross}}(r)}{n^{\text{par}}(r)} \tag{14}$$

The coefficient K, a calibration constant accounting for the difference in the responses of the two channels, is chosen in order to obtain the theoretical value to be expected from the atmosphere in a region where the aerosol contribution to the backscattering can be considered negligible (Young, 1980). In our case, this theoretical value was set to 0.014 (Behrendt et al., 2002). However, there may be an important source of systematic error in depolarization measurements that comes from the incomplete separation of parallel and cross polarized lidar returns, which leads to a mixing or a "cross talk" between receiving channels. The cross talk can be taken into account and different methods have been envisaged to properly assess it (Biele et al., 2000; Reichardt et al., 2003; Alvarez et al., 2006); in our case we estimated the cross talk following the approach outlined in (Snels et al., 2009) and the volume depolarization profiles are corrected accordingly (Cairo et al., 1999) for a cross talk of 2.5 % between channels. This level of incomplete splitting is in good accordance with what directly tested in our optic laboratory on the polarization beamsplitter cube used in our system.

2.6 Electromagnetic and mechanical compatibility

The system was tested at the Laboratory for Electromagnetic Fields ENEA Casaccia, in order to characterize the emissions radiated and conducted, to check the compatibility of its use on an airplane. The tests were conducted in more sessions in the period from June to July and November 2010. At the end of the test series, it has been certified (Test Report ENEA EMFLab April 2010 EMFLab and May 2010) that the lidar system

AMTD
5, 1253–1292, 2012

emits conducted and radiated noise levels below the limits prescribed by the relevant legislation. Therefore, it meet the requirements of MIL-STD 461E CE102 and RE102 for the tests.

3 Performances during flight

The system has been deployed in four flight tests on a C27-J Spartan of the italian Aeronautica Militare, all of them in daylight conditions. In the first flight the system was not operative, and was subjected to intense mechanical stresses to verify the solidity of installation and to control the maintenance of the optical alignment after the flight. In the subsequent sections, data from the flights when the system was operative are presented and discussed.

3.1 9 December 2010

The system was equipped with an ancillary computer dedicated to store the data acquired from the avionics sensors of the C27-J (geo-reference, time, aircraft altitude, atmospheric dynamical and thermodynamical parameters, acquired at 1 Hz) that were then used to interpret the lidar data. The parameters of the acquisition were set at 15 m vertical resolution for the current mode and 30 m vertical resolution for the photoncounting mode, the profiles extending respectively for 15 km and 30 km. The flashlamp laser power was set to 90 % of its maximum value. The integration time for each profile was set to 5 s. The aircraft took off from the Aeronautica Militare military base of Pratica di Mare (40.66° N, 12.48° E, 89 m a.s.l.) and headed south to fly over the CNR-IMAA CIAO atmospheric observatory of Potenza (40.60° N, 15.72° E, 760 m a.s.l.) (Madonna et al., 2011) to obtain simultaneous measurements with a ground based reference system of proven accuracy (Mona et al., 2009). Unfortunately, low cloudiness above the station did not allow to operate the ground based system. However, RAMNI collected data throughout the flight, that was performed at a constant altitude of 2150 m. The

AMTD
5, 1253–1292, 2012

flight altitude was dictated by the fact that the lidar faces the outside from an open hatch on the fuselage ceiling, so that the aircraft flew unpressurized. The data obtained allowed us to assess the system performances, even in absence of a ground based comparison. Here, only data from the 532 nm channels will be discusses, since the 1064 nm channel was affected by a noise that prevented a quantitative determination of the backscattering at this wavelenght. The source of this noise was not found in the timeframe of the project. However, the 1064 nm data qualitatively confirmed the 532 nm observations.

Figure 2 shows the color coded profiles of the total backscattering coefficient (aerosol + molecular) and Fig. 3 shows the volume depolarization, measured during the flight. Each profile represent an average over 5 s. Noticeable is the presence of scattered clouds at 4 km and 6 km altitude (the black areas where the data are outside the color scale), some of them optically so thick to inhibit the signal detection beyond them (at 57 000 s, 57 800 s, 58 200 s, 58 600 s). The low value of the depolarization suggests a liquid or mixed phase for them. Other high-altitude ice clouds, discernible from the high values of depolarization associated to them, are present around 10 km. The data collected during this flight, representative of an average background aerosol presence in an otherwise clear atmosphere, have been used to evaluate the sensitivity of the system when flying in daylight conditions, which are the most burdensome for lidars, by using the results of the uncertainty analysis reported in Sect. 2.4. Figure 4 displays two curves showing the distance from the aircraft vs the value of the aerosol backscatter coefficient that gives a signal to noise ratio equal to one. The black line is for an integration time of 5 s, the red line is for 60 s. Considering an aircraft speed of about 400 km h^{-1}, those integration times allow horizontal resolution of respectively 0.5 km and 3 km along the line of flight. The dotted line in Fig. 4 shows the molecular backscatter coefficient, computed from temperature and pressure measured by an atmospheric sounding at Pratica di Mare. The graph then allows an estimation of the minimum detectable value of the aerosol backscatter coefficient, as a function of the distance from the flight platform, in the worst measurement conditions, i.e. in daylight.

AMTD
5, 1253–1292, 2012

As instance, at 8000 m from the aircraft flying at 2000 m, for an integration time of 5 s, the signal to noise ratio equal one is reached for an aerosol backscatter coefficient of 0.5 Mm^{-1} sr^{-1}, i.e. for a total backscatter ratio of 2 at 10 km altitude; for an integration time of 60 s, the signal to noise ratio equal one is obtained for an aerosol backscatter coefficient of approximately 0.05 Mm^{-1} sr^{-1}, i.e. for a total backscatter ratio of 1.1 at 10 km altitude.

3.2 14 January 2011

The third flight aimed at monitoring the volcanic plume originated from a brief eruptive episode of the Etna volcano (37.73° N, 15.00° E, 3329 m a.s.l.). The Etna started on 12 January a strombolian activity with explosive outbursts of pasty lava ejected a few tens or hundreds of meters into the air, the activity becoming stronger during the night. On the 14, there was no activity responsible for lava emissions as in the previous day, and during our flight the volcano had already finished erupting since a few hours and only a plume of water vapor and gases persisted from the mouth of the volcano, pushed south south-westward by the prevailing winds. Figure 5 show the Aerosol Optical Depth (left panel) and Angstom coefficient (right panel) as measured by MODIS-Terra at 12:10 UT on the 14. The circle highlight the region where the plume originated from the volcano, was seeked for during the flight. The volcanic plume is hardly discernible in the Optical Depth image, a little more so in the Angstrom coefficient image where a zone of reduced values can be noticed, spreading from the south-western part of the coast of Sicily, toward the Strait of Sicily, advected by the wind that blowed almost perpendicular to the coastline.

The C27J took off from Pratica di Mare in the early afternoon and headed southward, making a transept parallel to the southwest sicilian coastline flying over the Strait of Sicily, at an altitude of about 1000 m, a few tens of kilometers from the land. The aircraft passed below the plume originating from the volcano which was situated at an altitude of about 2–3000 m. The plume was detected approx. 150 km downwind from the source, and was subvisible. The plane flew at a minimum distance of about 1000 m

AMTD
5, 1253–1292, 2012

from the base of the plume, that was considered to be a safe distance. Figures 6 and 7 show the color coded time series of profiles of total backscatter coefficient and depolarization – this latter extending only up to 4 km of altitude, because of high sky background - measured during the flight. Each profile represent an average over 5 s. The data clearly shows the presence of a layered structure of particulates that extends between 2 and 3.5 km, visible between the 55 000 s and 56 000 s. The origin of this structure was easily traced back to emissions from Etna, by inspecting the analysis of high altitude winds. The lack of any depolarization in the backscattered light suggests that the particles were essentially liquid, probably sulfate particles condensed from water vapor and minor gases emitted from Etna, with no detectable presence of large ash particles or soot. Lidar observaton for a similar event, performed in 2002 from the lidar station in Potenza, also reported the dominant presence of submicron sulfate particles (Villani et al., 2006). A zoom on the volcanic plume is reported on Fig. 8, where the aerosol backscatter ratio is presented. There, clearly discernible is the structure of the PBL, extending to 1000–1500 m – quite high for a marine PBL, so likely influenced by the transport off the coast, the noticeable presence of free tropospheric aerosols up to 5–6 km, and the elongated structure of the plume, with backscatter ratio as high as 4 in its higher portion.

On its way back along the south-east coast of the island, the plane flew close to Mount Etna and the pilot took pictures of the plume originating from its mouth, as displayed in Fig. 9.

3.2.1 28 May 2001

The flight was motivated by the forecast of the VAAC MetOffice announcing the presence of volcanic aerosol over the Po valley, above 11 km altitude and with concentrations ranging between 200 and 2000 $\mu g\,m^3$, as a result of the transport of the plume originated from the ongoing eruption of the Icelandic volcano Grimsvotn (63.98° N, 19.70° W). The presence of ashes was forecasted to occur between 06:00 UTC and 12:00 UTC. The C27J took-off from Pratica di Mare at 08:03 LT (06:03 UTC). The

AMTD
5, 1253–1292, 2012

aircraft followed a route toward the western end of the Po Valley, at an altitude of 1800 m , which was considered safe for flight, and began taking lidar measurements at 07:29 UTC, after an eastward turn, following the course of the river Po until it reached the Adriatic coast. There, climbed to 3200 m at 08:30 UTC, and turned south-southeast continuing the flight along the Adriatic coastline. The lidar measurements continued until the aircraft reached Ancona, then were shut off. The aircraft then came back to Pratica di Mare where it landed after about 4 flight hours.

The high altitude of the supposed ash presence, and the order of magnitude of the aerosol backscatter coefficients to be expected, ranging from 2 to 20 $Mm^{-1}\,sr^{-1}$, producing a lower limit for the Aerosol Backscatter Ratio of 5 at 12 km, posed this mission within the limit of our detection capabilities. Figures 10 and 11 report the color coded profiles of the total backscattering coefficient and volume depolarization, this time averaged over 60 s. The data collected show the presence of layers of tropospheric aerosol from the flight level up to to about 7 km, with values ranging from 0.1 to 0.3 $10^{-3}\,km^{-1}\,sr^{-1}$. These layers show a maximum depolarization at around 7 km, which decreases downward. Above this layered structure, the aerosol is significantly reduced. Above 9 km, no presence of aerosols is detected, with backscatter coefficient values above the 0.2 $Mm^{-1}\,sr^{-1}$ lower limit indicated by the VAAC forecast. This lack of aerosol presence received an indirect confirmation by lidar data from a CALIPSO satellite overpass (not shown), that crossed our aircraft trayectory at 12:36 UTC, and reported no aerosol presence.

4 Conclusions

An airborne lidar was prepared and tested as a tool for monitoring the presence and estimate the mass of particulates in the atmosphere. Three test flight have been performed, under conditions of high sky brightness. In one case, a volcanic plume originated from Etna volcano was detected, and presence of ashes was excluded. In a

AMTD
5, 1253–1292, 2012

different case, the system was able to exclude the presence of ashes that were forecated at concentrations considered hazardous to air traffic.

Appendix A

Eye safety concerns

The value of the Maximum Permissible Exposure (MPE) for a pulsed laser radiation depends on various parameters such as the emitted wavelength, the pulse repetition frequency (F), the duration of single pulse (t), the total duration of the pulse train (T), and the total exposure time (T_{max}). There are three separate criteria to be fulfilled, namely:

1. the MPE/pulse is limited by its value for each single pulse (single pulse limit),
2. the M MPE/pulse is limited by its value for all exposure times between T and T_{max}, divided by the number of pulses N during this time period (average power limit),
3. the MPE/pulse is limited by its value for a single pulse, multiplied by $N^{-1/4}$ where N the number of pulses that occur over time T_{max} (repetitive pulse limit),

and the enforced MPE is the lowest among those identified by these criteria.

Let $T_{max} = 0.25$ s be the time to close the eyes dazzled by a casual exposure to visible laser radiation (blink effect time). For a repetition frequency of 1 kHz, this physiological response time of the human eye to dazzling light gives $N = 250$. In Table 1, the MPE limits in the enforced legislation are reported. If the emission takes place simultaneously on more wavelengths, the MPE is additive.

In table the maximum allowable values are reported. The most compelling criterion appears to be the third. Using Eq. (1), the safety condition for the eyes (eye safety) is verified for $r \geq 1500$ m.

AMTD
5, 1253–1292, 2012

Acknowledgements. The authors express their sincere thanks to Gerardo De Canio, Alessandro Zambotti and the staff of the Laboratory of Qualification of Materials, Components and Systems of ENEA for the great willingness to collaborate in the project; to the Department of Earth and Environment of the National Research Council for financial support; to Gelsomina Pappalardo and the staff of CNR-IMAA for their availability to validate the system and for useful discussions on the interpretation of the data, and finally, to the italian Aeronautica Militare, and in particular the Reparto Sperimentale Volo, for uninterrupted support, contribution and great professionalism displayed in bringing to a successful end the system deployment in a short time.

References

Ansmann, A., Riebesell, M., and Weitkamp, C. : Measurement of atmospheric aerosol extinction profiles with a Raman lidar, Opt. Lett. 15, 746–748, 1990. 1266

Ansmann, A., Tesche, M., Groß, S., Freudenthaler, Seifert, V. P., Hiebsch, A., Schmidt, J., Wandinger, U., Mattis, I., Müller, D., and Wiegner, M.: The 16 April 2010 major volcanic ash plume over central Europe: EARLINET lidar and AERONET photometer observations at Leipzig and Munich, Germany, Geophys. Res. Lett., 37, L13810, doi:10.1029/2010GL043809, 2010. 1255, 1266

Ansmann, A., Tesche M., Seifert, P., Groß, S., Freudenthaler, V., Apituley, A., Wilson, K. M., Serikov, I., Linné, H., Heinold, B., Hiebsch, A., Schnell, F., Schmidt, J., Mattis, I., Wandinger, U., and Wiegner, M.: Ash and fine-mode particle mass profiles from EARLINET-AERONET observations over central Europe after the eruptions of the Eyjafjallajökull volcano in 2010, J. Geophys. Res., 116, D00U02, doi:10.1029/2010JD015567, 2011. 1255

Alvarez, J. M., Vaughan, M. A., Hostetler, C. A., Hunt, W. H., and Winker, D. M.: Calibration technique for polarization-sensitive lidars, J. Atmos. Ocean. Technol. 23, 683–699, 2006. 1267

Behrendt, A. and Nakamura, T. : Calculation of the calibration constant of polarization lidar and its dependency on atmospheric temperature, Opt. Exp., 10, 805–817, 2002. 1267

Biavati, G., Di Donfrancesco, G., Cairo, F., and Feist, D. G. : Correction scheme for close-range lidar returns, Appl. Opt., 50, 5872–5882, 2011. 1265

AMTD

5, 1253–1292, 2012

Biele, J., Beyerle, G., and Baumgarten, G.: Polarization lidar: corrections of instrumental effects, Opt. Exp. 7, 427-435, 2000. 1267
Böckmann, C., Wandinger, U., Ansmann, A., Bösenberg, J., Amiridis, V., Boselli, A., Delaval, A., De Tomasi, F., Frioud, M., Grigorov, I. V., Hågård, A., Horvat, M., Iarlori, M., Komguem, L., Kreipl, S., Glarchevêque, G., Matthias, V., Papayannis, A., Pappalardo, G., Rocadenbosch, F., Rodrigues, J. A., Schneider, J., Shcherbakov, V., and Wiegner, M.: Aerosol Lidar Intercomparison in the Framework of the EARLINET Project. 2. Aerosol Backscatter Algorithms, Appl. Opt., 43, 977–989, 2004. 1263
Bukowiecki, N., Zieger, P., Weingartner, E., Jurányi, Z., Gysel, M., Neininger, B., Schneider, B., Hueglin, C., Ulrich, A., Wichser, A., Henne, S., Brunner, D., Kaegi, R., Schwikowski, M., Tobler, L., Wienhold, F. G., Engel, I., Buchmann, B., Peter, T., and Baltensperger, U.: Ground-based and airborne in-situ measurements of the Eyjafjallajökull volcanic aerosol plume in Switzerland in spring 2010, Atmos. Chem. Phys., 11, 10011–10030, doi:10.5194/acp-11-10011-2011, 2011. 1255
Cairo, F., Di Donfrancesco, G., Adriani, A., Pulvirenti, L., and Fierli, F.: Comparison of Various Linear Depolarization Parameters Measured by Lidar, Appl. Opt., 38, 4425–4432,1999. 1267
Cavalieri, O., Cairo, F., Fierli, F., Di Donfrancesco, G., Snels, M., Viterbini, M., Cardillo, F., Chatenet, B., Formenti, P., Marticorena, B., and Rajot, J. L.: Variability of aerosol vertical distribution in the Sahel, Atmos. Chem. Phys., 10, 12005–12023, doi:10.5194/acp-10-12005-2010, 2010. 1256
Cavalieri, O., Di Donfrancesco, G., Cairo, F., Fierli, F., Snels, M., Viterbini, M., Cardillo, F., Chatenet, B., Formenti, P., Marticorena, B., and Rajot, J. L.: The AMMA MULID network for aerosol characterization in West Africa, Int. J. Remote Sens., 32, 5485–5504, doi:10.1080/01431161.2010.502156, 2011. 1256
Chazette, P., Sanak, J., and Dulac, F.: New Approach for Aerosol Profiling with a Lidar Onboard an Ultralight Aircraft: Application to the African Monsoon Multidisciplinary Analysis, Environ. Sci. Technol., 41, 8335–8341, doi:10.1021/es070343y, 2007. 1255
Chen, W. N., Chiang, C. W., and Nee, J. B.: The lidar ratio and depolarization ratio for cirrus clouds, Appl. Opt., 41, 6470–6497, 2002. 1266
Di Liberto, L., Angelini, F., Pietroni, I., Cairo, F., Di Donfrancesco, G., Viola, A., Argentini, S., Fierli, F., Gobbi, G., Maturilli, M., Neuber, R., and Snels, M.: Estimate of the Arctic planetary boundary layer height by a micro Lidar: a case study, Ad. Met., in press, 2012. 1256
di Sarra, A., Di Iorio T., Cacciani M., Fiocco G., and Fua, D.: Saharan dust profiles measured

AMTD
5, 1253–1292, 2012

by lidar from Lampedusa, J. Geophys. Res., 106, 10335–10347, 2001. 1267
Donovan, D. P., Whiteway, J. A., and Carswell, A. I.: Correction for nonlinear photon-counting effects in lidar systems, Appl. Opt., 32, 6742–6753, 1993. 1264
Flamant, C., Pelon, J., Chazette, P., Trouillet, V., Quinn, P., Frouin, R., Bruneau, D., Leon, J.-F., Bates, T., Johnson, J., and Livingstone, T.: Airborne lidar measurements of aerosol spatial distribution and optical properties over the Atlantic Ocean during a European pollution outbreak of ACE-2, Tellus, 52B, 662–677, 2000. 1254
Iwasaka, Y., Shibata, T., Nagatani, T., Shi, G.-Y., Kim, Y. S., Matsuki, A., Trochkine, D., Zhang, D., Yamada, M., Nagatani, M., Nakata, H., Shen, Z., Li, G., Chen, B., and Kawahiraand, K.: Large depolarization ratio of free tropospheric aerosols over the Taklamakan desert revealed by lidar measurements: possible diffusion and transport of dust particles, J. Geophys. Res., 108, 8652, doi:10.1029/2002JD003267, 2003. 1267
Immler, F. and Schrems, O.: Vertical profiles, optical and microphysical properties of Saharan dust layers determined by a ship-borne lidar, Atmos. Chem. Phys., 3, 1353–1364, doi:10.5194/acp-3-1353-2003, 2003. 1266
Klett, J. D.: Stable analytical inversion solution for processing lidar returns, Appl. Opt. 20, 211–220, 1981. 1266
Lilley, M., Lovejoy, S., Strawbridge, K., and Schertzer, D.: 23/9 dimensional anisotropic scaling of passive admixtures using lidar data of aerosols, Phys. Rev., Phys. Rev., E70, 3, 7 pp., 2004. 1254
Madonna, F., Amodeo, A., Boselli, A., Cornacchia, C., Cuomo, V., D'Amico, G., Giunta, A., Mona, L., and Pappalardo, G.: CIAO: the CNR-IMAA advanced observatory for atmospheric research, Atmos. Meas. Tech., 4, 1191–1208, doi:10.5194/amt-4-1191-2011, 2011. 1268
Marenco, F., Santacesaria, S., Bais A., F., Balis, D., di Sarra, A., Papayannis, A., and Zerefos, C.: Optical properties of tropospheric aerosols determined by lidar and spectrophotometric measurements (Photochemical Activity and Solar Ultraviolet Radiation campaign), Appl. Opt., 36, 6875–6886 1997. 1266
Marenco, F., Johnson, B., Turnbull, K., Newman, S., Haywood, J., Webster, H., and Ricketts, H.: Airborne lidar observations of the 2010 Eyjafjallajokull volcanic ash plume, J. Geophys. Res., 116, D00U05, doi:10.1029/2011JD016396, 2011. 1255
Mattis, I., Ansmann, A., Muller, D., Wandinger, U., and Althausen, D.: Dual wavelength Raman lidar observations of the extinction-to backscatter ratio of Saharan dust, Geophys. Res. Lett., 29, 1306, doi:10.1029/2002GL014721, 2002. 1266

AMTD
5, 1253–1292, 2012

Moerl, P., Reinhardt, M. E., Renger, W., and Schellhase, R.: The use of the airborne lidar ALEX-F for aerosol tracing in the lower troposphere, Contr. Atmas. Phys., 45, 403–410, 1981. 1254

Mona, L., Pappalardo, G., Amodeo, A., D'Amico, G., Madonna, F., Boselli, A., Giunta, A., Russo, F., and Cuomo, V.: One year of CNR-IMAA multi-wavelength Raman lidar measurements in coincidence with CALIPSO overpasses: Level 1 products comparison, Atmos. Chem. Phys., 9, 7213–7228, doi:10.5194/acp-9-7213-2009, 2009. 1268

O'Connor, E. J., Illingworth, A. J., and Hogan, R. J.: A technique for autocalibration of cloud lidar, J. Atmos. Ocean Tech., 21, 777–786, 2004. 1266

Petersen, G. N.: A short meteorological overview of the Eyjafjallajokull eruption 14 April-23 May 2010, Weather, 65, 203–207, 2010. 1255

Reichardt, J., Baumgart, R., and McGee, T. J.: Three signal method for accurate measurements of depolarization ratio with lidar, Appl. Opt., 42, 4909–4913, 2003. 1267

Renger, W., Kiemle, C., Schreiber, H. G., Wirth, M., and Morl, P.: Correlative measurements in support of LITE using the airborne backscatter lidar ALEX, in: Advances in Atmospheric Remote Sensing with Lidar, edited by: Ansmann, A., Neuber, R., Rairoux, P., and Wandinger, U., Springer-Verlag, Berlin, 165–168, 1997. 1254

Sassen, K. : The polarization lidar technique for cloud research: a review and current assessment, B. Am. Meteorol. Soc., 72, 1848–1866, 1991. 1267

Schumann, U., Weinzierl, B., Reitebuch, O., Schlager, H., Minikin, A., Forster, C., Baumann, R., Sailer, T., Graf, K., Mannstein, H., Voigt, C., Rahm, S., Simmet, R., Scheibe, M., Lichtenstern, M., Stock, P., Rüba, H., Schäuble, D., Tafferner, A., Rautenhaus, M., Gerz, T., Ziereis, H., Krautstrunk, M., Mallaun, C., Gayet, J.-F., Lieke, K., Kandler, K., Ebert, M., Weinbruch, S., Stohl, A., Gasteiger, J., Groß, S., Freudenthaler, V., Wiegner, M., Ansmann, A., Tesche, M., Olafsson, H., and Sturm, K.: Airborne observations of the Eyjafjalla volcano ash cloud over Europe during air space closure in April and May 2010, Atmos. Chem. Phys., 11, 2245–2279, doi:10.5194/acp-11-2245-2011, 2011. 1255

Snels, M., Cairo, F., Colao, F., and Di Donfrancesco, G.: Calibration method for depolarization lidar measurements, Int. J. Remote Sens., 30, 5725–5736, doi:10.1080/01431160902729572, 2009. 1267

Stachlewska, I. S., Neuber, R., Lampert, A., Ritter, C., and Wehrle, G.: AMALi – the Airborne Mobile Aerosol Lidar for Arctic research, Atmos. Chem. Phys., 10, 2947–2963, doi:10.5194/acp-10-2947-2010, 2010. 1254, 1280

AMTD
5, 1253–1292, 2012

Russell, P. B., Swissler, T. J., and McCormick, M. P.: Methodology for error analysis and simulation of lidar aerosol measurements, Appl. Opt. 18, 3783–3797, 1979. 1260, 1263

Villani, M. G., Mona, L., Maurizi, A., Pappalardo, G., Tiesi, A., Pandolfi, M., DIsidoro, M., Cuomo, V., and Tampieri, F.: Transport of volcanic aerosol in the troposphere: The case study of the 2002 Etna plume, J. Geophys. Res., 111, D21102, doi:10.1029/2006JD007126, 2006. 1271

Wandinger, U., Muller, D., Bockmann, C., Althausen, D., Matthias, V., Bosenberg, J., Weiss, V., Fiebig, M., Wendisch, M., Stolhl, A., and Aansmann, A.: Optical and microphysical characterization of biomass-burning and industrial-pollution aerosols from multi wavelength lidar and aircraft measurements, J. Geophys. Res., 107, 8125, doi:10.1029/2000JD000202, 2002. 1266

Young, A. T.: Revised depolarization corrections for atmospheric extinction, Appl. Opt., 19, 3247–3248, 1980. 1267

AMTD

5, 1253–1292, 2012

Table 1. Synopsis of the system specifications.

Technical specifications of the RAMNI system	
Detected Wavelengths	1064, 608 and 532 nm (two ploarizations)
Laser Type	Nd-YAG (1064 and 532 nm)
Pulse duration	1 ns
Laser repetition rate	up to −1 kHz
Laser output energy	0.8 mJ at 1064 nm; 0.35 mJ at 532 nm
Telescope diameter	20 cm
Telescope type	F/1.5 Newtonian
Telescope field of view	0.7 mrad
Beam divergence	0.4 mrad, full angle x 7 expanded
Filter Bandwidth	2 nm
Vertical Resolution	From 7.5 to 150 in photoncounting mode From 1.875 to 15 m in current mode
Vertical range	1024 x Vertical Resolution
Time resolution	down to 1 s

AMTD
5, 1253–1292, 2012

Table 2. Values of the MPE for direct eye exposure to laser radiation, according to Sicherheitstechnischen Festlegungen und Anlagen fr Lasergerate, VDE 1998 Beuth-Verlag, ISSN 0178-224X (Stachlewska et al., 2010).

	Criterion 1	Criterion 2	Criterion 3
Emission duration	10^{-9}–10^{-7} s	10^{-9}–10^{-7} s	10^{-3}–10 s
Wavelength 315–400 nm	$5.6\,t^{0.25}\,10^{3}\,Jm^{-2}$	$5.6\,t^{0.25}\,10^{3}\,Jm^{-2}$	–
Wavelength 400–550 nm	$5\,10^{-3}\,Jm^{-2}$	$18\,t^{0.75}\,Jm^{-2}$	$N^{-0.25}\cdot 5\,10^{-3}\,Jm^{-2}$
Wavelength 1050–1150 nm	$5\,10^{-2}\,Jm^{-2}$	$90\,t^{0.75}\,Jm^{-2}$	$N^{-0.25}\cdot 5\,10^{-2}\,Jm^{-2}$

AMTD
5, 1253–1292, 2012

Table 3. Maximum permittible exposure for our system.

	532 nm	1064 nm	tot
MPE_1	$5 \cdot 10^{-3}\,Jm^{-2}$	$50 \cdot 10^{-3}\,Jm^{-2}$	$55 \cdot 10^{-3}\,Jm^{-2}$
MPE_2	$6.4 \cdot 10^{-3}\,Jm^{-2}$	$31.8 \cdot 10^{-3}\,Jm^{-2}$	$38.2 \cdot 10^{-3}\,Jm^{-2}$
MPE_3	$1.25 \cdot 10^{-3}\,Jm^{-2}$	$12.5 \cdot 10^{-3}\,Jm^{-2}$	$13.75 \cdot 10^{-3}\,Jm^{-2}$

AMTD
5, 1253–1292, 2012

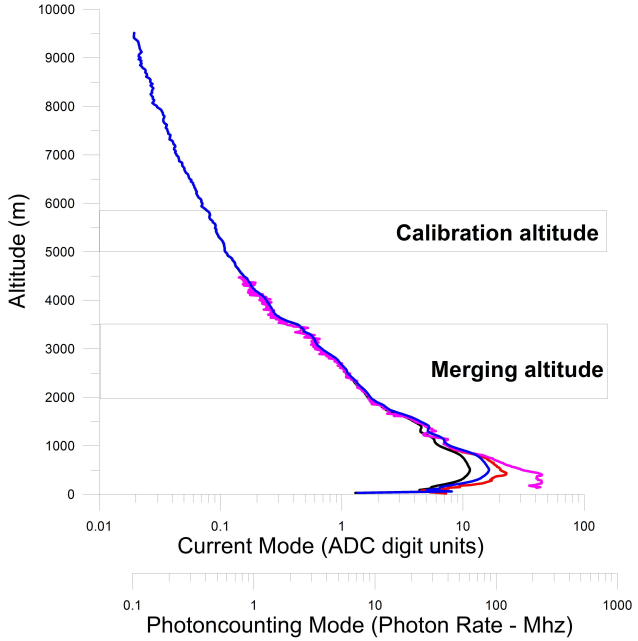

Fig. 1. Atmospheric backscatter return. Photon counting acquisition, before (black) and after (blue) dead time correction. Current acquisition, before (red) and after (purple) partial overlap correction. The data were acquired on 7 December 20:20 UTC, and represent (photoncounting) or are proportional (current) to the photon flux induced by a single laser shot.

AMTD
5, 1253–1292, 2012

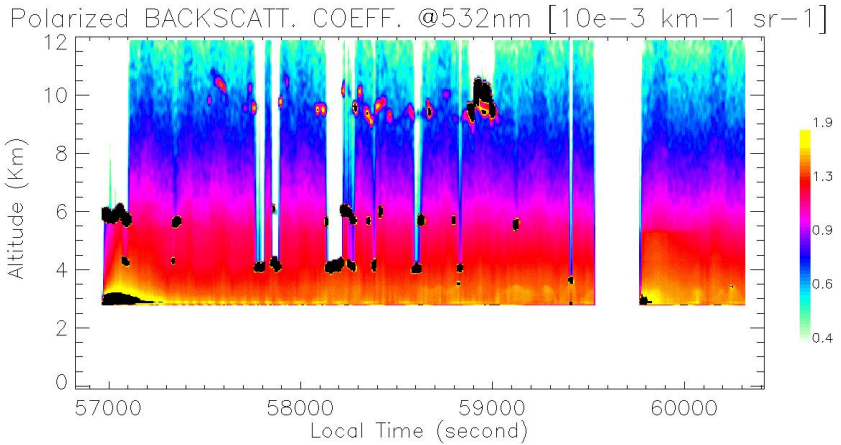

Fig. 2. Time vs altitude curtain of total (aerosol + molecular) backscatter coefficient, for the flight on 9 December 2010.

AMTD
5, 1253–1292, 2012

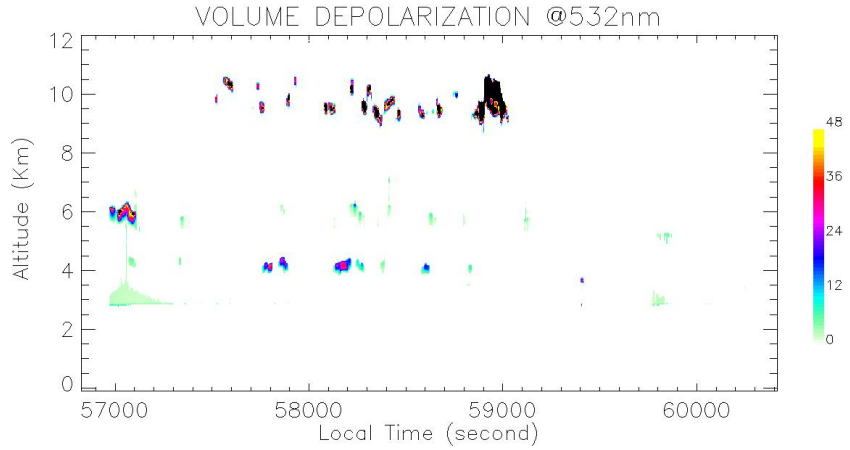

Fig. 3. Time vs. altitude curtain of total depolarization ratio, for the flight on 9 December 2010.

AMTD
5, 1253–1292, 2012

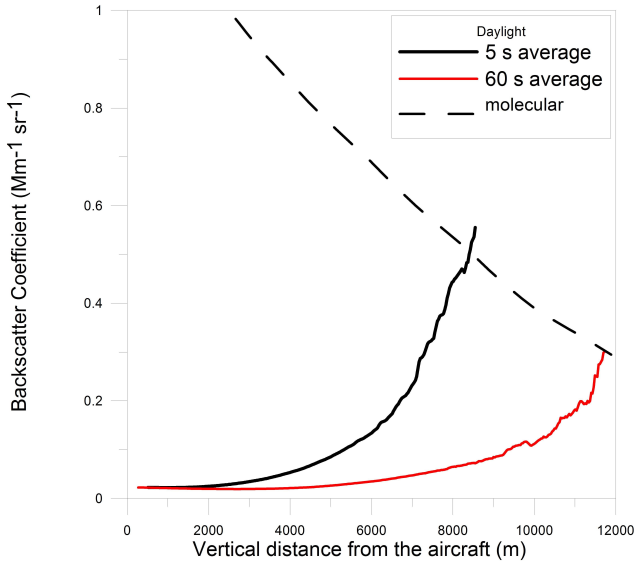

Fig. 4. Curves of signal to noise ratio equal to one, function of the distance from the aircraft, and of the aerosol backscatter coefficient. The black line is for 5 s integration time, the red is for 60 s integration time. the dotted line represent the molecular backscatter coefficient values. These curves were computed from the data from the first flight of RAMNI, when the aircraft was flying at 2150 m altitude.

AMTD
5, 1253–1292, 2012

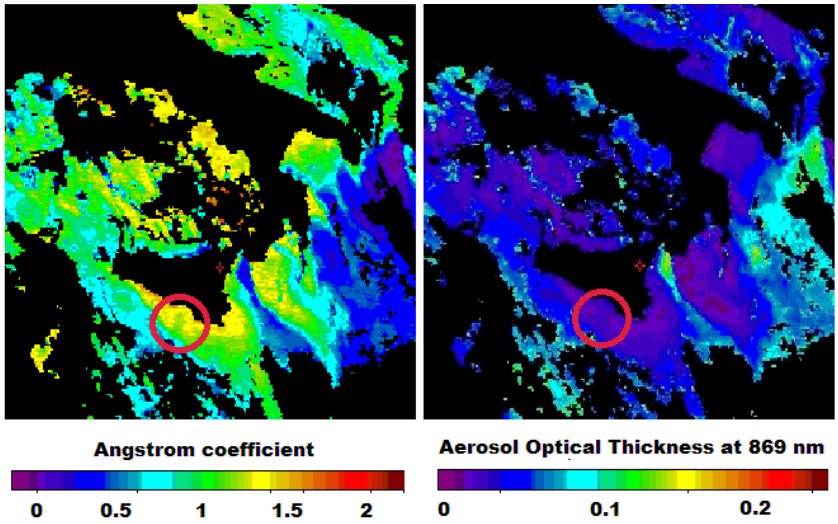

Fig. 5. Color coded Aerosol Optical Depth (left panel) and Angstrom coefficient (right panel) by MODIS Terra, on 14 December 2010 at 12:10 UT. The circles highlight where the an enchancement of AOD and a variation of the Angstrom coefficient with respect to its background values can be discerned, originated by the volcanic plume from Etna. The star show the position of the volcano.

AMTD
5, 1253–1292, 2012

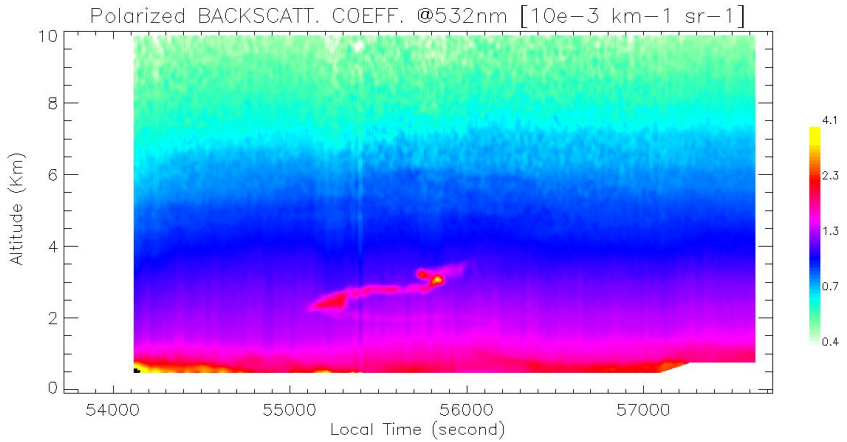

Fig. 6. Time vs. altitude curtain of total backscatter coefficient, for the flight on 14 January 2011.

AMTD
5, 1253–1292, 2012

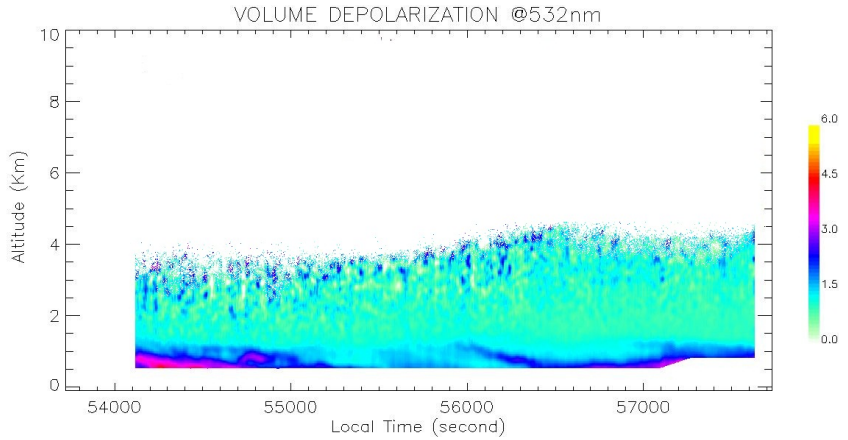

Fig. 7. Time vs. altitude curtain of total depolarization ratio, for the flight on 14 January 2011.

AMTD
5, 1253–1292, 2012

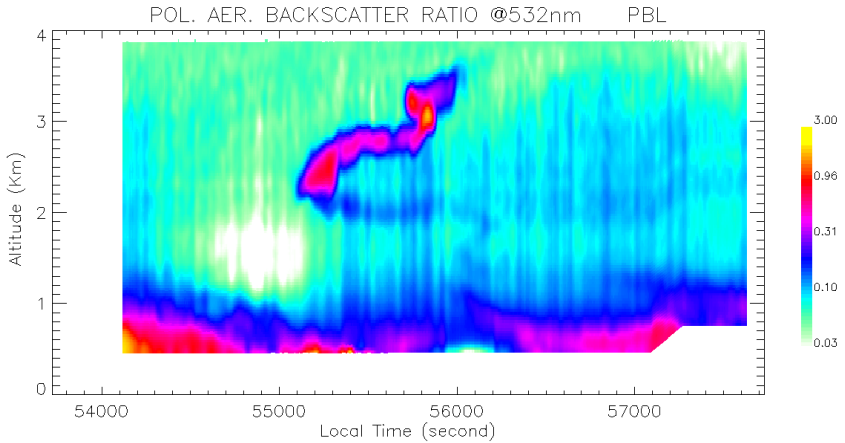

Fig. 8. Time vs. altitude curtain of aerosol backscatter coefficient, for the flight on 14 January 2011.

AMTD
5, 1253–1292, 2012

Fig. 9. A picture of Mount Etna taken on 14 January from onboard the C27J- Spartan aircraft (courtesy T. Col. F. Palazzi).

AMTD
5, 1253–1292, 2012

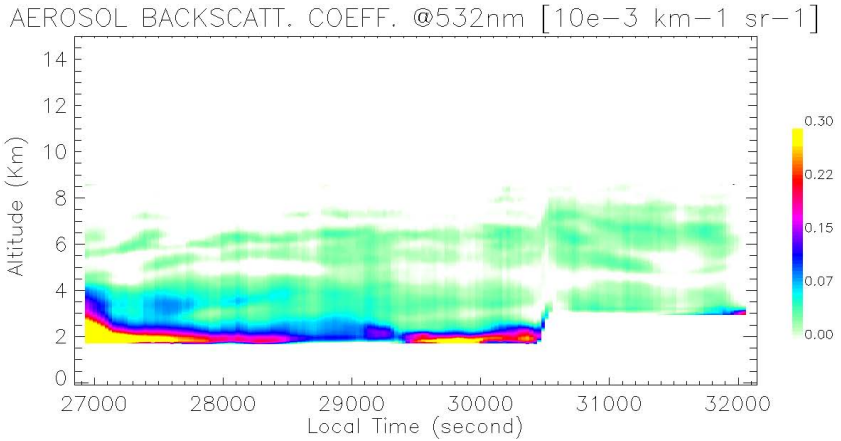

Fig. 10. Time vs. altitude curtain of aerosol backscatter coefficient, for the flight on 28 May 2011.

AMTD
5, 1253–1292, 2012

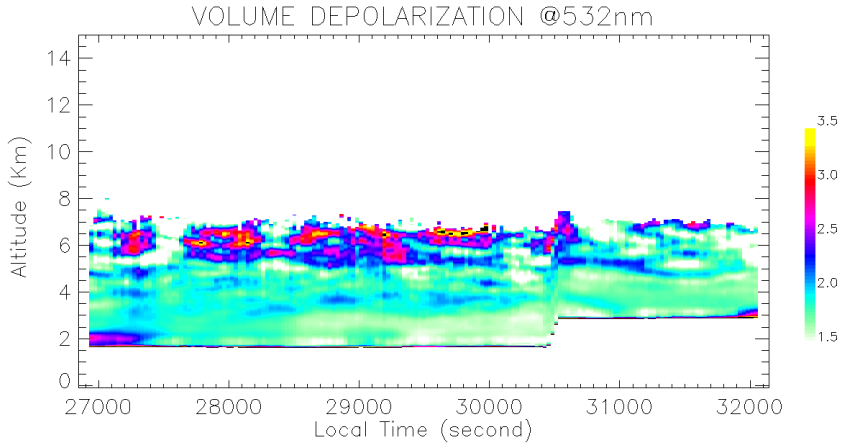

Fig. 11. Time vs. altitude curtain of total depolarization ratio, for the flight on 28 May 2011.

AMTD
5, 1253–1292, 2012